



## PARTICLE FRACTURE SIMULATION IN NON-UNIFORM MICROSTRUCTURES OF METAL–MATRIX COMPOSITES

S. GHOSH and S. MOORTHY

Department of Aerospace Engineering, Applied Mechanics and Aviation, The Ohio State University, Columbus, OH 43210, U.S.A.

(Received 5 May 1997; accepted 5 August 1997)

**Abstract**—This paper deals with the evolution of damage in microstructures of reinforced ductile-matrix composites, by particle cracking and splitting. A small deformation Voronoi Cell finite element model is developed, in which each element may consist of a matrix phase, an inclusion phase and a crack phase. Brittle inclusions may be of arbitrary shapes and sizes, and may be dispersed non-uniformly in the matrix. Damage initiation of inclusions is assumed to follow a maximum principal stress theory. Complete particle cracking or splitting is assumed at the onset of damage. The model is validated by a few comparison studies. Various geometric patterns are studied to test the effectiveness of the model, as well as to understand the effect of morphology on damage evolution. Actual microstructures from optical micrographs of Al–Si–Mg composite systems are analyzed and compared with experimentally observed results. Quantitative characterization and statistical analysis is conducted to correlate morphological parameters with mechanical response. © 1998 Acta Metallurgica Inc.

### 1. INTRODUCTION

The presence of fibers or particulates in composite microstructures often has adverse effects on their failure properties like fracture toughness, ductility and creep resistance. Important micromechanical phenomena that are responsible for deterring the overall properties include, fracture and splitting of reinforcements, matrix failure and inclusion–matrix debonding. Many engineering materials exhibit strong non-uniformities in inter-particle/fiber spacings, inclusion shapes, volume fractions and arrangements, at the microstructural level. In addition, there are heterogeneities at larger length scales which include local regions of clustering and directionality, often related to the fabrication process. Failure characteristics of heterogeneous materials are affected by microstructural mechanisms that control initiation and evolution of localized damage and cracks. These mechanisms are highly sensitive to local parameters, such as reinforcement distribution, morphology, size, interfacial strength etc. Experimental studies with MMCs [1] have established that particles in regions of clustering or preferential alignment, have a greater propensity towards fracture, than those in regions of dilute concentration. SEM micrographs of damaged MMCs show that larger particles tend to fracture at lower macroscopic load levels due to the existence of large flaws. Christman *et al.* [2] have shown that local plastic flow is very sensitive to shape of reinforcements. Lack of reliability of these composite materials has inhibited their applications to high performance load carrying engineering components. It is therefore important to understand damage

mechanisms and fracture process for enhancing the level of utilization of these material systems.

Within the framework of damage mechanics, micromechanical damage models have been employed to predict overall constitutive response by using continuum mechanics principles at the microscopic level [3, 4]. While some of these models [3] provide reasonable predictions of overall properties for a dilute distribution of damage entities, others [4] attempt to analyze the interaction effects between damage entities introduced by morphological characteristics of the microstructure. Recently, novel approaches to integrate micromechanical and computational approaches at the microscale with phenomenological approaches in the macroscale have also been proposed [5]. While many of these methods can model damage in brittle homogeneous materials, far fewer analytical models are available for ductile two phase materials. Small scale yielding solutions using asymptotic analysis for a single bi-material interface due to Shih and Asaro [6] and Hutchinson *et al.* [7] are notable exceptions.

Evolving damage in heterogeneous media with a mixture of ductile and brittle constituents have been numerically modeled using *Unit Cell* methods. These methods assume that the material is constituted of periodic repetition of unit cells, identified as representative volume elements (RVE) of the microstructure. Displacement based finite element analysis is used to analyze the RVE in order to predict the onset and growth of evolving damage. Notable among these are the finite element simulations by Needleman [8, 9], Tvergaard [10], Bao [11], Hom [12], Sugimura *et al.* [13] and Finot *et al.* [14].

In Refs [10–13], simple microstructures with pre-existing damaged heterogeneities are considered. In Ref. [14] a finite element mesh which allows for crack growth by element separation is used to simulate microscale particle and matrix cracking. While these models provide valuable insights into the microstructural damage processes, the simple morphologies idealize actual microstructures for many engineering materials. Consideration of simple RVEs bears little relationship to the actual stereographic features, and has limited them to the assumption that all particles or particle/matrix interfaces are *damaged simultaneously*. To circumvent these deficiencies, Suresh and coworkers [15,2], McHugh *et al.* [16] among others, have made novel progresses in computational modeling of discontinuously reinforced materials with random spatial dispersion. However, a very high resolution of finite element mesh is required even for undamaged heterogeneous media, and enormous computational efforts are required to capture failure by these models.

The microstructure based *Voronoi Cell Finite Element Model (VCFEM)* developed by Ghosh *et al.* [17,18], has shown a significant promise in this regard. It can overcome the large computational requirements of conventional finite element methods, by combining concepts of hybrid finite elements with characteristics of micromechanics. The VCFEM mesh naturally evolves from the microstructure by Dirichlet tessellation to generate a network of multi-sided *Voronoi polygons*. Each Voronoi cell represents a basic structural element containing one second phase inclusion at most (see [19] for details), and the analysis needs no further discretization leading to drastically reduced efforts in generating the microstructural mesh. Additionally, computational efficiency is greatly enhanced due to Voronoi cell elements being considerably larger than conventional unit cell finite elements, with reduced degrees of freedom.

The evolution of damage by particle cracking or splitting, in particle reinforced ductile matrix microstructures, is analyzed in this paper by a Voronoi cell finite element model. No matrix cracking is allowed in this paper. Each Voronoi cell element may consist of a matrix phase, an inclusion phase and a crack phase. The inclusions are brittle, of arbitrary shapes and sizes, and may be dispersed non-uniformly in the matrix. Damage initiation is assumed to follow a maximum principle stress theory or Rankine criterion. Complete particle cracking or splitting is assumed at the onset of damage. Different geometric patterns are studied to test the effectiveness of the model, as well as to understand the effect of morphology on damage evolution. Actual microstructures from optical micrographs of Al–Si–Mg composite systems are analyzed and compared with experimentally observed results. Quantitative characterization and statistical analysis is conducted to correlate morphological parameters with mechanical response.

## 2. VORONOI CELL FEM WITH PARTICLE FRACTURE

The Voronoi cell finite element model has been developed for undamaged composite and porous materials in Refs [17,18] using the assumed stress hybrid formulation. The formulation is extended to accommodate damage evolution in the form of particle cracking or splitting. It is assumed that in particle cracking, the crack is completely contained within the inclusion, while for particle splitting its tip extends nominally into the matrix. The crack in a fractured particle is realized as an elliptical void with a high aspect ratio ( $\sim 10$ – $100$ ), implying a blunt crack. Each Voronoi cell element is amenable to change in topology from two constituent phases (matrix and inclusions) in undamaged cells, to three phases (matrix, inclusion and crack) in damaged cells. Complete particle cracking or splitting is assumed to occur at the very onset of damage, and thus the problem of crack propagation within each inclusion is avoided. This assumption is justifiable from the consideration that for the multitude of inclusions analyzed, crack propagation in each inclusion would make the problem inordinately large. Additionally, experimental observations indicate rapid transition from crack initiation to complete cracking/splitting.

### 2.1. Voronoi cell element formulation for damage

Consider a typical representative material element (RME) consisting of  $N$  undamaged and/or damaged particles, that are contained in each of the  $N$  Voronoi cell elements as shown in Fig. 5(a). The assumed stress hybrid formulation in the Voronoi cell finite element method (VCFEM) requires independent assumptions of an equilibrated stress field ( $\sigma$ ) in the interior of each element  $\Omega_e$  and compatible displacement fields  $\mathbf{u}$  on the element boundary  $\partial\Omega_e$ ,  $\mathbf{u}^*$  on the matrix–inclusion interface  $\partial\Omega_e$  and  $\mathbf{u}^*$  on the crack boundary  $\partial\Omega_{cr}$ . In an incremental formulation for elasto-plasticity, the incremental two field ( $\sigma$ – $\mathbf{u}$ ) hybrid variational formulation introduces an element energy functional,

$$\begin{aligned} \Pi_e^C(\Delta\sigma, \Delta\mathbf{u}) &= - \int_{\Omega_e} \Delta B(\sigma, \Delta\sigma) d\Omega - \int_{\Omega_e} \varepsilon : \Delta\sigma d\Omega \\ &+ \int_{\partial\Omega_e} (\sigma + \Delta\sigma) \cdot \mathbf{n}^e \cdot (\mathbf{u} + \Delta\mathbf{u}) \partial\Omega \\ &- \int_{\Gamma_{in}} (\bar{\mathbf{t}} + \Delta\bar{\mathbf{t}}) \cdot (\mathbf{u} + \Delta\mathbf{u}) d\Gamma \\ &- \int_{\partial\Omega_e} (\sigma^m + \Delta\sigma^m - \sigma^c - \Delta\sigma^c) \cdot \mathbf{n}^c \cdot (\mathbf{u}' + \Delta\mathbf{u}') \partial\Omega \\ &- \int_{\partial\Omega_{cr}} (\sigma^c + \Delta\sigma^c) \cdot \mathbf{n}^{cr} \cdot (\mathbf{u}'' + \Delta\mathbf{u}'') \partial\Omega \end{aligned} \quad (1)$$

where  $\Delta B$  is the increment of complimentary energy

density. Variables  $(\sigma, \mathbf{u})$  correspond to values at the beginning of an increment, while variables  $(\Delta\sigma, \Delta\mathbf{u})$  are the corresponding increments in a load increment or step. Outward normals on  $\partial\Omega_e$ ,  $\partial\Omega_c$  and  $\partial\Omega_{cr}$  are denoted by  $\mathbf{n}^e$ ,  $\mathbf{n}^c$  and  $\mathbf{n}^{cr}$ , respectively. Superscripts m, c and cr are associated with the matrix, inclusion and crack phases, respectively, in each Voronoi cell element. The total energy for the entire RME of  $N$  Voronoi cells is obtained as  $\Pi^C = \sum_{e=1}^N \Pi_e^C$ . Setting the first variation of  $\Pi^C$  in equation (1) with respect to stress increments  $\Delta\sigma$  to zero yields the element compatibility as the Euler equation, while setting the first variations of  $\Pi^C$  with respect to the independent boundary displacements  $\Delta\mathbf{u}$ ,  $\Delta\mathbf{u}'$  and  $\Delta\mathbf{u}''$  to zero, yield the inter-element traction reciprocity or element boundary traction, interface traction reciprocity and zero traction on crack boundary, respectively. Equilibrated stress increments  $\Delta\sigma$ , compatible displacement fields  $\Delta\mathbf{u}$ ,  $\Delta\mathbf{u}'$  and  $\Delta\mathbf{u}''$ , the stress-strain relationships ( $\frac{\partial \Delta B}{\partial \Delta \sigma} = \Delta \epsilon$ ), along with the Euler equations completely define the incremental problem for a heterogeneous RME.

## 2.2. Element assumptions

Independent assumptions on stress increments  $\Delta\sigma$  are made in the matrix and inclusion phases in each element, thus allowing stress discontinuities across the interface. In two-dimensional analysis, the Airy's stress function  $\Phi(x, y)$  is usually convenient in deriving equilibrated stress fields. Components of  $\Delta\sigma$  are expressed in terms of  $\Phi$  as:

$$\Delta\sigma_{xx} = \frac{\partial^2 \Phi}{\partial y^2}, \quad \Delta\sigma_{yy} = \frac{\partial^2 \Phi}{\partial x^2}, \quad \Delta\sigma_{xy} = -\frac{\partial^2 \Phi}{\partial x \partial y} \quad (2)$$

Incorporation of key features of micromechanics in the choice of stress functions significantly enhances computational efficiency. Moorthy and Ghosh [17, 19] have introduced a decomposition of the matrix and inclusion stress functions into (a) purely polynomial functions  $\Phi_{poly}^m$ ,  $\Phi_{poly}^c$  and (b) reciprocal functions  $\Phi_{rec}^m$ ,  $\Phi_{rec}^c$  and  $\Phi_{rec}^{cc}$ , for elements with matrix, inclusion and crack phases. Mathematically, the stress functions for the matrix and inclusion phases are constructed as:

$$\begin{aligned} \Phi^m &= \Phi_{poly}^m + \Phi_{rec}^m + \Phi_{rec}^{mc} \\ \Phi^c &= \Phi_{poly}^c + \Phi_{rec}^{cc} \end{aligned} \quad (3)$$

In the above equation, the purely polynomial part of the stress functions  $\Phi_{poly}^{m/c}$  accounts for the far field tractions on the element boundary  $\partial\Omega_e$  and on the interface  $\partial\Omega_c$ , and are expressed as:

$$\Phi_{poly}^{m/c} = \sum_{p,q} \xi^p \eta^q \Delta\beta_{pq}^{m/c} \quad (4)$$

where  $(\xi, \eta)$  are the scaled local coordinates with origin at the element centroid  $(x_c, y_c)$ , and may be written as  $\xi = (x - x_c)/L$ ,  $\eta = (y - y_c)/L$ .  $L$  is a

scaling parameter  $(= \sqrt{\max(x - x_c) \max(y - y_c)}) \forall (x, y) \in \partial\Omega_e$ . The use of the local coordinates  $(\xi, \eta)$  prevents numerical inaccuracies in  $\Phi^{m/c}$  due to high exponents of  $(x, y)$ , and thus avoids ill-conditioning of the element stiffness matrices. The reciprocal terms  $\Phi_{rec}^m$ ,  $\Phi_{rec}^{mc}$  and  $\Phi_{rec}^{cc}$  facilitate stress concentration near the interface and crack boundary, accounting for the shape of the inclusion and crack. They also help satisfy traction reciprocity (zero traction for the crack) at the interfaces  $\partial\Omega_c$  and  $\partial\Omega_{cr}$ , as well as decay at large distances from these interfaces. The matrix reciprocal function  $\Phi_{rec}^m$  is constructed from a transformed radial coordinate  $f$ , that is generated by either a Schwarz–Christoffel conformal transformation (for elliptical heterogeneities) [20], or by a Fourier series transformation of the interface  $\partial\Omega_c$  (for arbitrary shapes) [17]. The radial distance  $f$  satisfies the conditions  $f \rightarrow \infty$  as  $(x, y) \rightarrow \infty$ , and  $f = 1$  on the interface  $\partial\Omega_c$ . In the expression for  $\Phi_{rec}^m$ , shape effects are dominant near  $\partial\Omega_c$  and vanish in the far-field.

$$\Phi_{rec}^m = \sum_{p,q} \xi^p \eta^q \sum_i \frac{1}{f^{p+q+i-1}} \Delta\beta_{pqi}^m \quad (5)$$

At the interface ( $f = 1$ ), coefficients  $\Delta\beta_{pqi}^m$  in equation (5) impart flexibility to the polynomial coefficients  $\Delta\beta_{pq}^m$  for matching traction conditions. Finally, the terms  $\Phi_{rec}^{mc}$  and  $\Phi_{rec}^{cc}$  are contributions to the matrix and inclusion stress functions due to the crack.

$$\begin{aligned} \Phi_{rec}^{mc} &= \sum_{p,q} \xi^p \eta^q \sum_i \left( \frac{\Delta\beta_{pqi}^{mc}}{f_{cr}^{p+q+i-1}} \right) \\ \Phi_{rec}^{cc} &= \sum_{p,q} \xi^p \eta^q \sum_i \left( \frac{\Delta\beta_{pqi}^{cc}}{f_{cr}^{p+q+i-1}} \right) \end{aligned} \quad (6)$$

The inclusion crack is assumed to be of elliptical shape with a high aspect ratio. Consequently, the crack boundary  $\partial\Omega_{cr}$  is parametrically represented through a conformal mapping of the ellipse as  $f_{cr}(x, y) = 1$ .  $f_{cr}$  represents a parameterized radial coordinate with the property  $f_{cr} \rightarrow \infty$  as  $(x, y) \rightarrow \infty$ . The reciprocal terms

$$\frac{1}{f_{cr}^{p+q+i-1}}$$

in  $\Phi_{rec}^{cc}$  facilitate zero traction condition on the crack boundary  $\partial\Omega_{cr}$ . The same terms  $\Phi_{rec}^{mc}$  provide asymptotic stress gradients near the crack tip in the matrix. Stress increments may be derived by substituting  $\Phi$  functions in the equation (2) in the form  $\{\Delta\sigma^m\} = [\mathbf{P}^m]\{\Delta\beta^m\}$  for the matrix and  $\{\Delta\sigma^c\} = [\mathbf{P}^c]\{\Delta\beta^c\}$  for the inclusion. All of the stress coefficients  $\{\Delta\beta^m\}$  and  $\{\Delta\beta^c\}$  are *a priori* unknown and are solved by setting the first variation of the element energy functional (1) with respect to the stresses to zero. Compatible displacement incre-

ments are generated on each of the boundaries/interfaces  $\partial\Omega_e$ ,  $\partial\Omega_c$  and  $\partial\Omega_{cr}$  by interpolation in terms of generalized nodal displacements as,

$$\begin{aligned} \{\Delta \mathbf{u}\} &= [\mathbf{L}^e] \{\Delta \mathbf{q}\} \quad , \quad \{\Delta \mathbf{u}'\} = [\mathbf{L}^c] \{\Delta \mathbf{q}'\} \quad , \\ \{\Delta \mathbf{u}''\} &= [\mathbf{L}^{cr}] \{\Delta \mathbf{q}''\} \end{aligned} \quad (7)$$

where  $\{\Delta \mathbf{q}\}$ ,  $\{\Delta \mathbf{q}'\}$  and  $\{\Delta \mathbf{q}''\}$  are the nodal displacement increment vectors, and  $[\mathbf{L}^e]$ ,  $[\mathbf{L}^c]$  and  $[\mathbf{L}^{cr}]$  are the corresponding interpolation matrices. In general, linear forms of  $[\mathbf{L}]$  are computationally efficient. However for the crack boundary, discontinuous normals at the nodes may degrade the solution and hence a quadratic interpolation is implemented. Details of the solution process are provided in [17, 19, 21].

### 2.3. Constitutive relations and particle cracking criterion

The reinforcing phase of particles are assumed to be brittle and are modeled as linear elastic materials. The matrix material on the other hand is assumed to be ductile, and is modeled by small deformation elasto-plasticity relations using associated  $J_2$  flow theory with isotropic hardening. For the brittle particulate materials, microstructural damage initiation is assumed to be governed by a maximum principle stress based criterion, also known as the Rankine criterion. In this criterion, a crack is initiated when the maximum principle stress in tension exceeds a critical fracture stress  $\sigma_{cr}$  at a point. In the computational procedure, complete particle cracking or splitting is assumed to occur in the form of an elliptical void, as soon as the principle tensile stress reaches  $\sigma_{cr}$ . In the case of particle cracking, the crack tip coincides with the interface and is completely contained in the particle, while it extends nominally into the matrix for particle splitting. A parameter

$$d_{crack} = \frac{\text{Crack Length}}{\text{Inclusion Dimension}}$$

distinguishes between complete cracking and splitting of inclusions. A fully cracked inclusion corresponds to a value  $d_{crack} = 1$ , for which the crack terminates at the inclusion–matrix interface, whereas splitting is represented by  $d_{crack} = 1.004$  for which the crack tip has moved slightly into the matrix. In the incremental computational procedure, more than one point may exceed the critical  $\sigma_{cr}$  value during increment. The location of a single crack is determined by a weighted averaging method as:

$$\begin{aligned} x_{\text{damage}} &= \frac{\sum x \frac{\sigma_1^c(x,y)}{\sigma_{cr}}}{\sum \frac{\sigma_1^c(x,y)}{\sigma_{cr}}} \quad , \\ y_{\text{damage}} &= \frac{\sum y \frac{\sigma_1^c(x,y)}{\sigma_{cr}}}{\sum \frac{\sigma_1^c(x,y)}{\sigma_{cr}}} \quad \forall [\sigma_1^c(x,y) \geq \sigma_{cr}] \end{aligned} \quad (8)$$

where  $\sigma_1^c(x,y)$  correspond to all values of maximum tensile principal stress larger than  $\sigma_{cr}$  in the particle. The crack is oriented at right angles to the principal stress directions at  $(x_{\text{damage}}, y_{\text{damage}})$  and extends to the interface on both sides.

**2.3.1. Critical fracture stress.** Various experimental studies on metal matrix composites [22–24], suggest that the critical stress  $\sigma_{cr}$  for particle fracturing is not only material dependent, but is also influenced by the particle size due to the existence of microcracks. Micrographs of damaged composites indicate that larger particles tend to fracture at lower load levels than smaller particles. To account for the size effect in particle cracking, and hence flaw size and distribution, two alternative approaches are considered. These criteria have been discussed in Curtin [25], Kiser *et al.* [24]. The first is a fracture mechanics based criterion, in which particles are assumed to contain flaws and the critical stress to fracture is determined from Mode-I fast fracture of these flaws. In this criterion, an initial particle flaw size  $c$  is assumed to be a fraction of a characteristic length  $D$ , and is expressed as  $c = eD$ . The characteristic length is considered to be the diameter of an equivalent circle or

$$D = \sqrt{\frac{4A}{\pi}},$$

where  $A$  is the particle area. The factor  $e$  is determined from experimental observations, and a value ~5–15% is found to be suitable in this study. For mode-I fracture, the critical load to fracture  $\sigma_{cr}$  is thus related to the fracture toughness  $K_{IC}$  through the relation:

$$\sigma_{cr} = \frac{K_{IC}}{\sqrt{\pi c}} = \frac{K_{IC}}{\sqrt{\pi e D}} \quad (9)$$

Larger particles with large initial flaws will fracture at smaller critical stresses by this relation. The second criterion uses statistical functions to correlate particle size, stress levels and failure. It is based on a Weibull distribution, in which the probability of particle fracture  $P_f(A, \sigma)$  is related to the particle volume (area in 2D)  $A$  and the maximum principal stress  $\sigma_1$  as:

$$P_f(A, \sigma) = 1 - e^{-A \left(\frac{\sigma_1}{\sigma_{cr}}\right)^m} \quad (10)$$

where  $\sigma_{cr}$  and  $m$  are two material parameters in the Weibull distribution. The probability of damage in this model, increases with larger particles at larger stress levels. The Weibull parameters  $\sigma_{cr}$  and  $m$  may be calculated by correlating geometric features and simulated stresses with experimental observations, as discussed in the section on numerical examples.

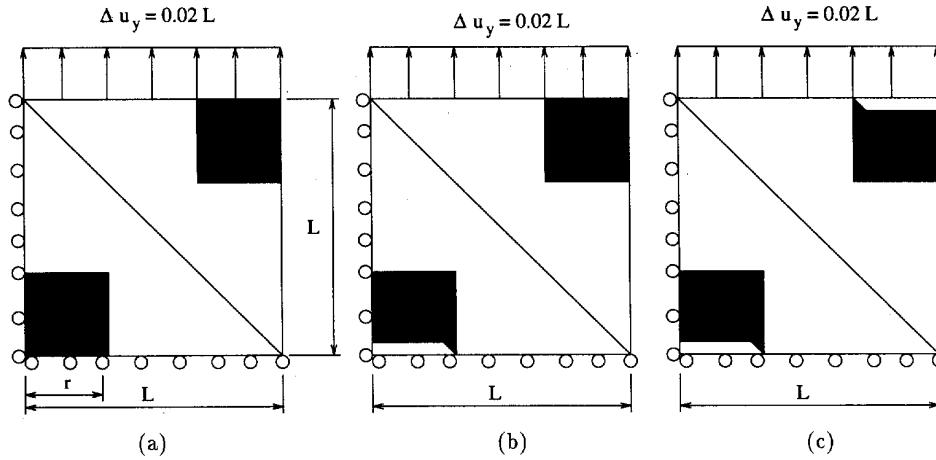


Fig. 1. Representation and VCFEM mesh for RME with  $V_f=20\%$  cracked square inclusions: (a) 0% damage, (b) 50% damage and (c) 100% damage.

### 3. VALIDATION EXAMPLES FOR VORONOI CELL FEM

The accuracy and efficiency of the Voronoi cell finite element model in stress analysis of heterogeneous materials with particle cracking has been extensively verified by comparison with results of analyses conducted with conventional finite element packages as well as with published results in the literature. Several comparison studies have been made with this model, some of which are described in [21,19]. Only one such example study with simple, uniform distribution is described here. To establish an aspect ratio for the elliptical cracks, a numerical experiment was conducted with various aspect ratios viz. ( $\frac{a}{b}=3, 5, 10, 25, 20$  and  $100$ ).

From this study, a ratio  $\frac{a}{b}=10$  was found to be most desirable from an efficiency and accuracy point of view. While both plane stress and plane strain problems have been solved, the numerical examples presented in this paper are only for the plane strain assumption.

#### 3.1. Square diagonal packing with existing crack

This comparison problem, studied by Finot *et al.* [14] with finite deformation kinematics, involves stress analysis of a square-diagonally packed composite microstructure with pre-cracked inclusions. The representative material element (RME) consists of two square SiC inclusions (volume fraction  $V_f=20\%$ ) in an Al-3.5% Cu matrix as

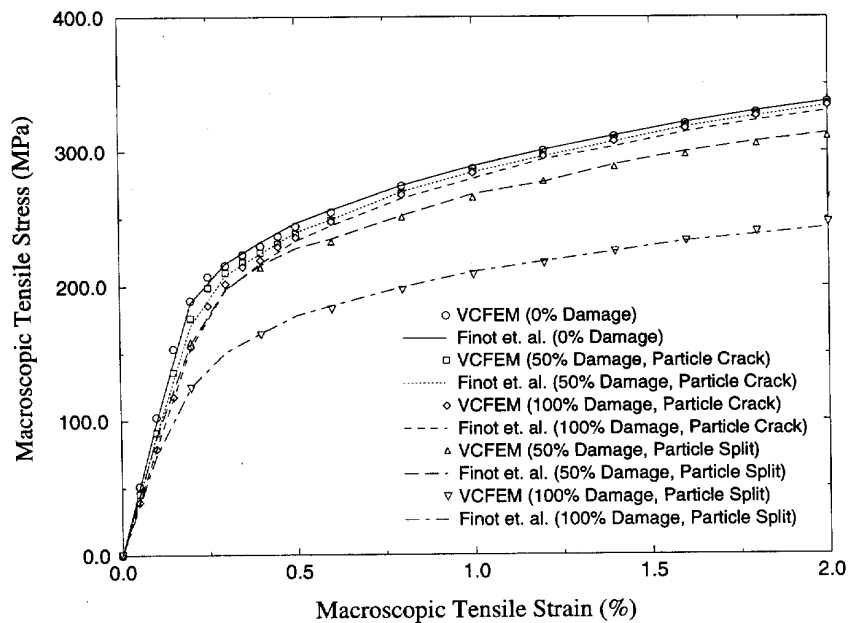


Fig. 2. Macroscopic stress-strain response for RMEs with  $V_f=20\%$  cracked square inclusions.

shown in Fig. 1. The elastic properties of SiC particles are assumed to be: Young's Modulus  $E = 450$  GPa and Poisson's Ratio  $\nu = 0.2$ . The elastic-plastic properties for the Al-3.5% Cu alloy matrix are taken as: Young's Modulus  $E = 72$  GPa, Poisson's Ratio  $\nu = 0.32$ ; Post yield behavior (Power law hardening)  $\sigma_m = \sigma_0(\epsilon_m^p/\epsilon_0 + 1)^N$ , with  $\sigma_0 = 175$  MPa, and  $N = 0.2$ . Different degrees of pre-existing damage, e.g. 0% damage with two intact inclusions, 50% damage with cracked inclusion, and 100% damage with both inclusions cracked, are assumed in accordance with those used in Ref. [14]. For 0% damage, the matrix stress function  $\Phi^m$  in equation (3) consists of 61 terms, with 25 polynomial terms  $\Phi_{\text{poly}}^m[p + q = 2..6$  in equation (4)] and 36 reciprocal terms  $\Phi_{\text{rec}}^m[i = 1..3, p + q = 2..4$  in equation (5)]. The corresponding inclusion stress

function  $\Phi^c$  in equation (3) consists of 25 polynomial terms  $\Phi_{\text{poly}}^c[p + q = 2..6$  in equation (5)]. The function  $f$  in equation (5) for  $\Phi_{\text{rec}}^m$  is created by a Fourier series transformation of the square interface, as described in Ref. [17]. For damaged microstructures, 36 additional terms in the form of  $\Phi_{\text{rec}}^{mc}$  and  $\Phi_{\text{rec}}^{cc}$  are appended to the stress functions  $\Phi^m$  and  $\Phi^c[i = 1..3, p + q = 2..4$  in equation (6)].

The VCFEM simulation of the RME is executed for up to a vertical applied strain of 2% as shown in Fig. 1. In Fig. 2 the macroscopic stress-strain responses, calculated by taking volumetric averages of microscopic variables, are compared with results in Ref. [14], and excellent agreement is recorded. The stress capacity of the RME reduces considerably with transition from particle cracking to particle splitting. As the crack propagates into the matrix

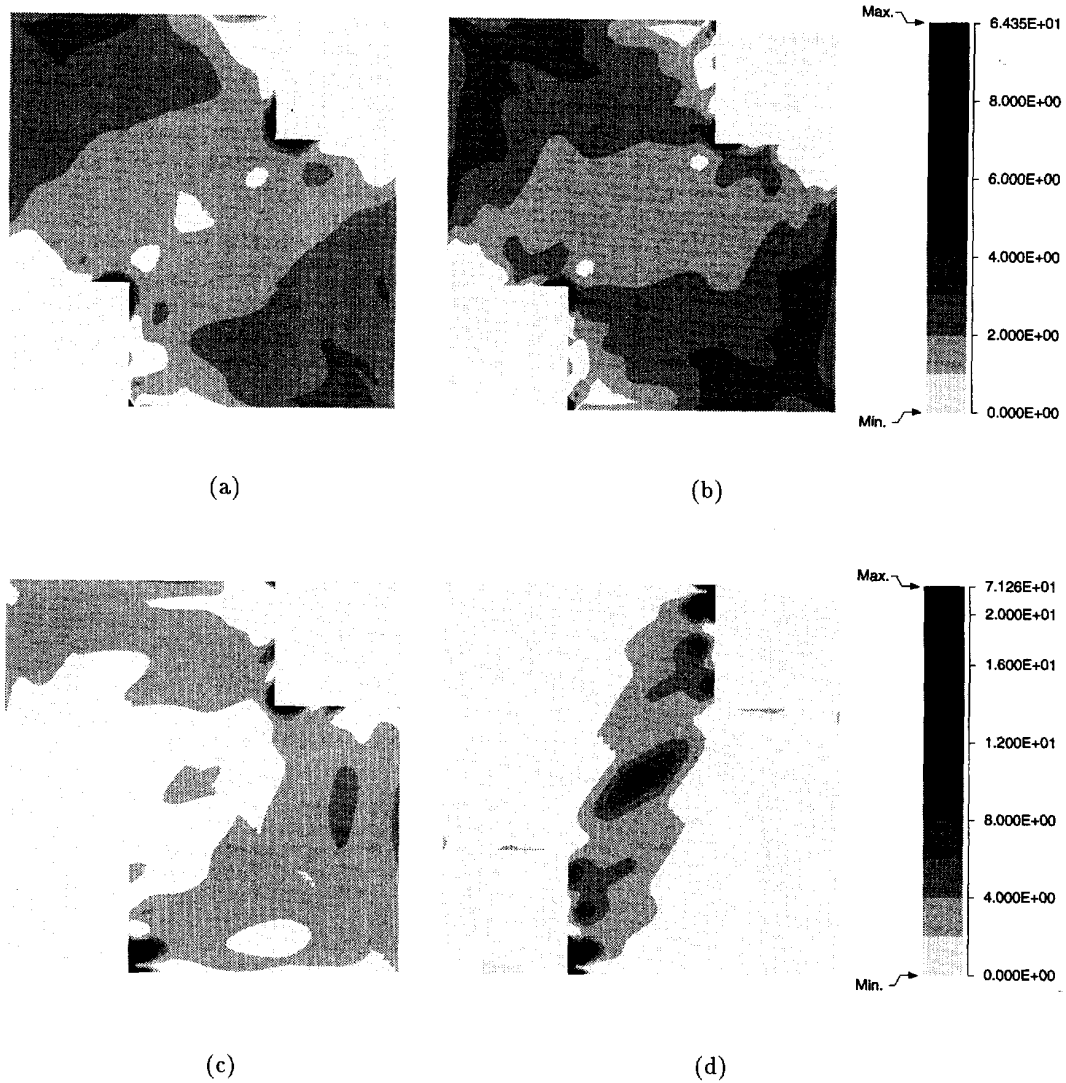


Fig. 3. Equivalent plastic strain (%) distribution at  $\bar{\epsilon}_{vv} = 2\%$  for (a) 50% cracked inclusion, (b) 100% cracked inclusion, (c) 50% split inclusion and (d) 100% split inclusions.

due to splitting, the damaged inclusions cease to carry significant load. The major load now shifts to the matrix material and the remaining undamaged inclusions. Contour plots of the effective plastic strains for the cracked and split microstructures at  $\bar{\epsilon}_{yy}=2\%$  are presented in Fig. 3. The matrix regions vertically adjacent to the split inclusions have considerably less plastic strain than those adjacent to cracked inclusions, due to much lower stresses caused by splitting. Also in the case of splitting, a considerably larger plastic strain accumulates near the crack tip. The plastic strain flows in the form of ligaments from one crack tip to the next, causing bands of strain localization. Similar observations have also been made in Ref. [14] for axisymmetric inclusions.

#### 4. DAMAGE IN NON-UNIFORM MICROSTRUCTURES

Examples in the previous section consider pre-existing damage, and thus do not involve crack initiation and change of element topology. The present section deals with continuously evolving microstructural topology through the onset and evolution of particle cracking in more complex, computer simulated and real microstructures. For undamaged Voronoi elements, the matrix function  $\Phi^m$  in equation (3) consists of 34 terms with 25 polynomial terms  $\Phi_{\text{poly}}^m[p + q = 2..6$  in equation (4)] and 9 reciprocal terms  $\Phi_{\text{rec}}^m[i = 1..3, p = 0..2, q = 2 - p$  in equation (5)]. The inclusion stress function  $\Phi^c$  consists of 25 polynomial terms  $\Phi_{\text{poly}}^m[p + q = 2..6$  in equation (5)]. Fewer reciprocal terms are used than in the previous example due to the smooth interface for circular inclusions. For cracked elements though, the additional reciprocal terms are the same as those in the previous example, i.e.  $[i = 1..3, p + q = 2..4$  in equation (6)].

##### 4.1. Computer simulated microstructures

The effect of particle clustering on damage evolution is studied with two computer generated microstructural distributions as follows.

(a) *A hard core distribution*: which is generated as a variant of a pure random Poisson pattern through the imposition of two constraints, namely (i) no two inclusions are allowed to overlap, and (ii) all inclusions are completely contained within the region window.

(b) *A single cluster hard core distribution*.

(c) *Triple cluster hard core model*, where clusters are characterized by reduced average inclusion separation distance in an otherwise hard-core region.

Each RME consists of 50 equi-sized circular Si particles dispersed in an Al-Si-Mg alloy matrix, and constituting a 20% volume fraction. Pertinent dimensions are: RME size =  $200 \mu \times 200 \mu$ , particle diameter =  $14.2 \mu$ , cluster diameter in (b) =  $33.38$

$\mu$  and cluster diameter in (c) =  $25.78 \mu$ . Details of the generation process are described in Ref. [27].

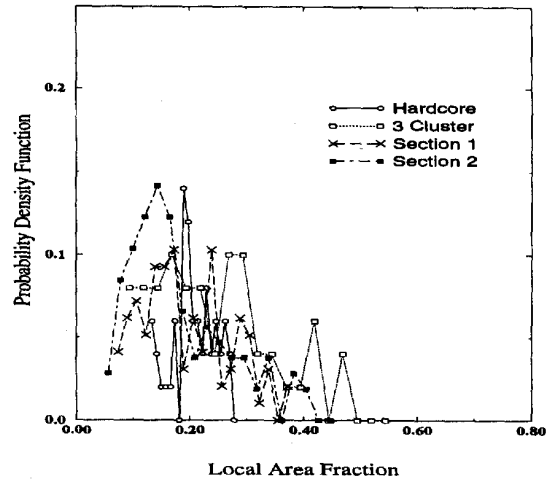
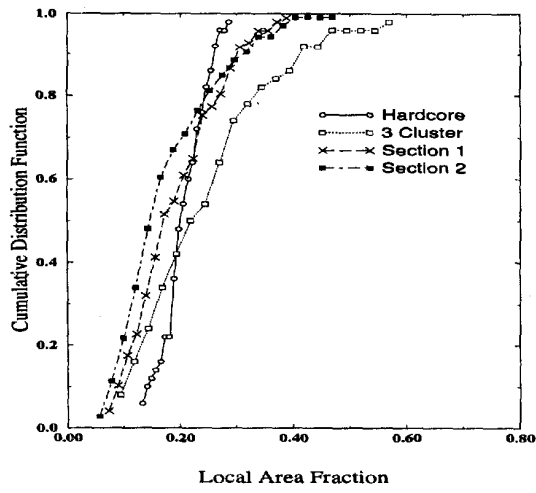
4.1.1. *Characterization*. Statistical functions of geometric descriptors, which can discriminate between patterns, as discussed in Refs [27, 28], are considered. Figures 4(a) and (b) show the cumulative distribution function  $F(A)$  and the probability density function  $f(A)$  of the local area fraction, measured as the ratio of the particle size to the area of the associated Voronoi cell. The range of  $A$  for hard core pattern is significantly shorter than for clustered patterns and thus the difference in  $F(A)$  increases with increasing area fraction. The high spike in  $f(A)$  for the hard-core pattern is a consequence of the steep gradients due to the pronounced uniformity in local area fraction, and the intensity of these spikes diminishes with clustering. The cumulative distribution function  $F(d)$  and density distribution functions  $f(d)$  for center to center nearest neighbor distances are plotted in Fig. 4(c) and (d). The longer plateaus in  $F(d)$  and the corresponding zeros in  $f(d)$  for clustered patterns are for the distances for which a near neighbor does not exist. Spikes in  $f(d)$  are much more pronounced for the hard-core distribution due to large number of neighbors at nearly similar distances. The lowest  $d$  values are much smaller for the clustered patterns. Second order intensity function  $K(r)$ , defined as the number of additional points expected to lie within a distance  $r$  of an arbitrarily located point divided by overall the point density, is an informative descriptor and has been discussed in [30, 27, 28]. Additionally, the pair distribution function of

$$g(r) = \frac{1}{2\pi r} \frac{dK(r)}{dr}$$

corresponds to the probability  $g(r)dr$  of finding an additional point within a circle of radius  $dr$  and centered at  $r$ . The two functions are plotted for the patterns in Fig. 4(e) and (f) and compared with a pure Poisson process for which  $K(r) = \pi r^2$  and  $g(r) = 1$ . With increase in clustering,  $K(r)$  deviates from that for the Poisson process. The peaks in  $g(r)$  are more pronounced for the hard core distribution indicating a greater likelihood of encountering additional particles at lower radii for this volume fraction.

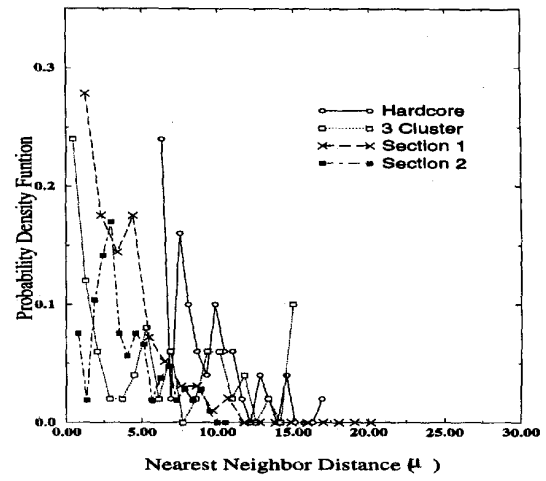
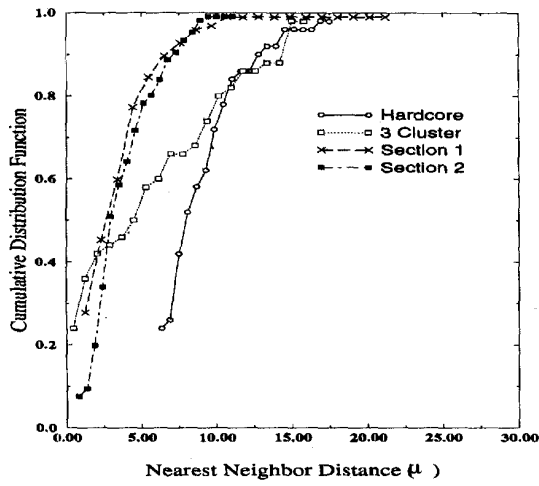
4.1.2. *Damage simulation*. Both complete particle cracking and particle splitting are analyzed in this example, with initially undamaged particles. Constituent material properties are as follows:

For the *Al-Si-Mg matrix*: Young's modulus  $E = 69$  GPa, Poisson's ratio  $\nu = 0.33$ , and post yield elastic-plastic behavior is obtained from data on B-treatment matrix material in Figs 5 and 1 (p. 137) of Hunt [22]. For the *Si inclusions*: Young's modulus  $E = 161$  GPa, Poisson's ratio  $\nu = 0.2$ . All particles are of identical shape and size, and therefore a constant critical stress to failure  $\sigma_{cr} = 300$  MPa is assumed. The RMEs are subjected to a



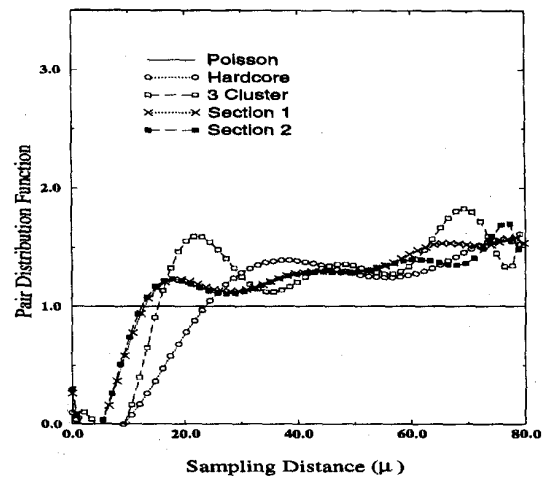
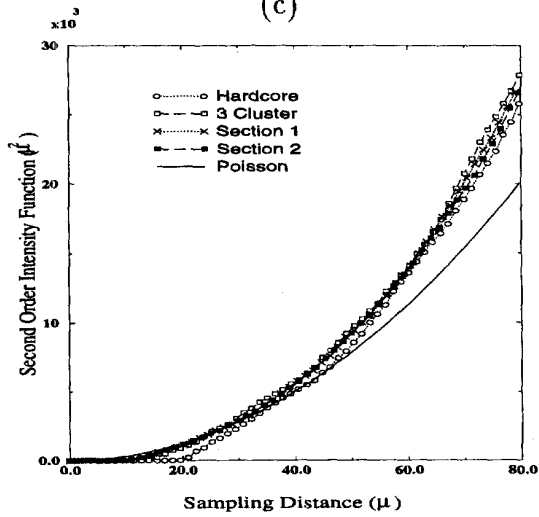
(a)

(b)



(c)

(d)



(e)

(f)

Fig. 4. (a) Cumulative distribution and (b) probability density functions of local area fractions; (c) cumulative distribution and (d) probability density functions of nearest neighbor distance; (e) second order intensity and (f) pair distribution functions for computer simulated and actual microstructures.



macroscopic horizontal tensile strain that increases from zero to a maximum of  $\bar{\epsilon}_{xx}=2\%$ . Evolving damaged configurations by particle splitting are shown in Fig. 5(a–f). For the hard core pattern, the first set of particles crack at  $\bar{\epsilon}_{xx}=0.6\%$ . Particle cracking occurs at random locations with increased loading up to a strain of  $\bar{\epsilon}_{xx}=1.6\%$ , after which no additional cracking is noticed. Large plastic strains occur in regions near the crack tips. However, due to the lack of close proximity of cracked particles,

plastic strain regions were not observed to propagate in any preferred direction. In contrast, for the triple cluster microstructure in Fig. 5(d–f), the first set of particles crack and split within the cluster near the top-right corner at  $\bar{\epsilon}_{xx}=0.4\%$ . With increased loading, high stress concentration at the crack tips lead to progressive cracking of other particles inside this cluster before particles in other clusters begin to crack. However, if only particle cracking is allowed, particles in both the top right

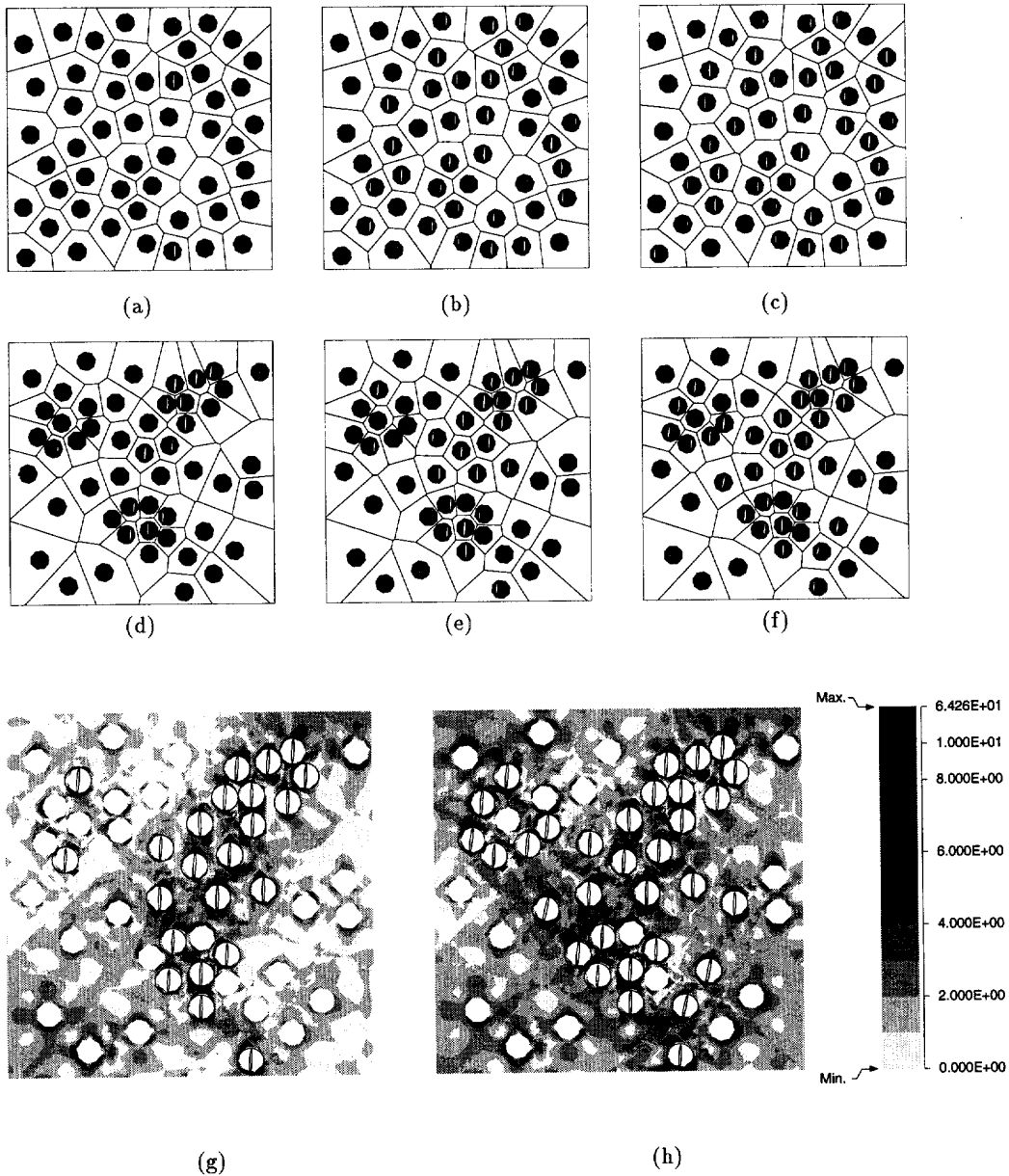


Fig. 5. Damage configurations of hard core microstructure at (a)  $\bar{\epsilon}_{xx}=0.8\%$ , (b)  $\bar{\epsilon}_{xx}=1.4\%$  and (c)  $\bar{\epsilon}_{xx}=2.0\%$ . Damage configurations of triple cluster microstructure at (d)  $\bar{\epsilon}_{xx}=0.8\%$ , (e)  $\bar{\epsilon}_{xx}=1.4\%$  and (f)  $\bar{\epsilon}_{xx}=2.0\%$ ; corresponding effective plastic strains (%) for triple cluster microstructure at (g)  $\bar{\epsilon}_{xx}=1.4\%$  and (h)  $\bar{\epsilon}_{xx}=2.0\%$ , for particle splitting with  $\sigma_{cr}=300$  MPa.

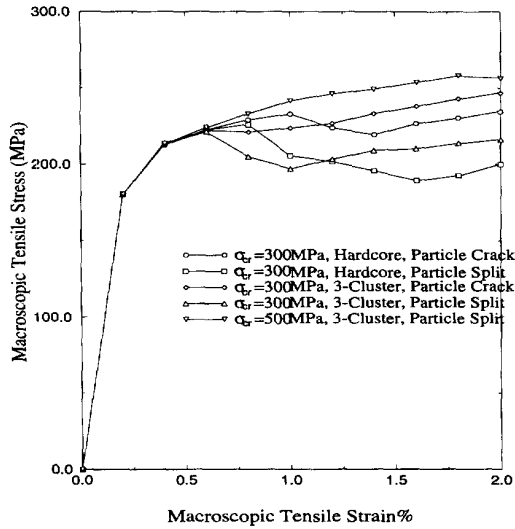
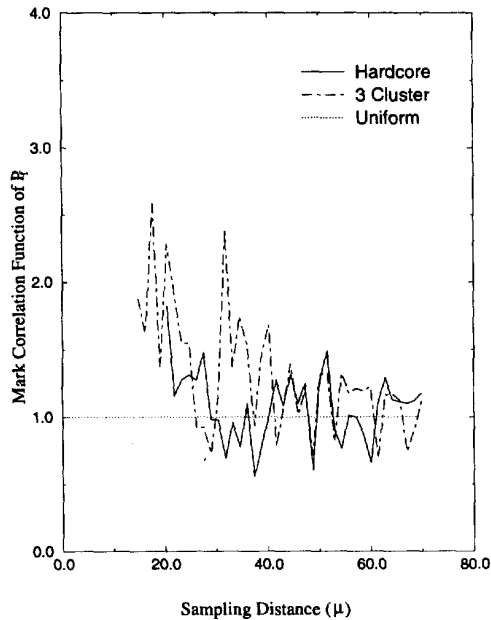


Fig. 6. Macroscopic stress-strain response for computer generated microstructures due to particle cracking and splitting.

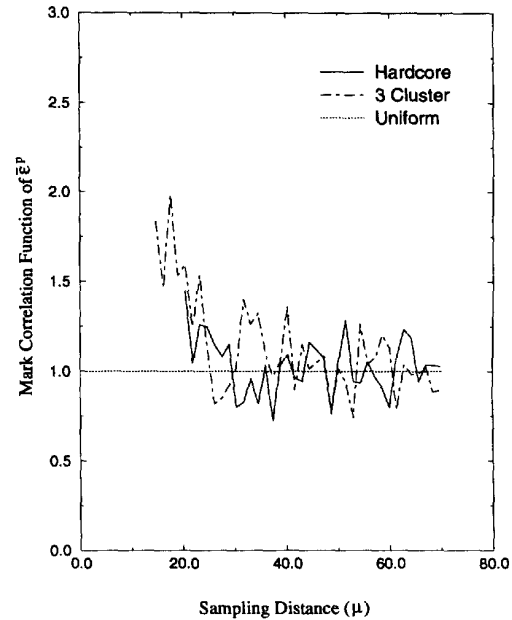
and bottom center clusters begin to crack almost concurrently. Particles in the third cluster remain relatively undamaged during the entire process. At the final strain  $\bar{\epsilon}_{xx} = 2.0\%$ , most particles in the two clusters are split while damage in the third cluster has just begun. During the initial stages of deformation and splitting, localized plastic straining

occurs in the top-right cluster which propagates from one crack tip to the next within the cluster by linking. Plastic straining in other clusters is less pronounced during this period. With subsequent particles splitting, plastic straining intensifies in bottom-center cluster and eventually links up with strained regions in the top cluster. High strain regions are much more diffused in the case of particle cracking and occur at higher macroscopic stresses compared to the particle splitting case.

Macroscopic stress-strain responses of the hardcore and triple clustered RMEs are illustrated in Fig. 6. Abrupt drops due to particle cracking are smoothed in this figure. The stress level for the hardcore pattern with particle splitting continues to drop throughout the loading. For the clustered microstructure, drops are higher in the initial stages due to rapid failure in the clusters, followed by increase in the stress levels due to matrix hardening. In general the RME with cracked particles projects a considerably stiffer behavior when compared to that with split particles. The effect of spatial distributions on damage evolution is studied through marked correlation functions  $M(r)$  introduced in Pyrz [30] and used in Refs [27,28]. Two marks associated with each particle are considered for their relevance to damage evolution. They are: (a) a parameter  $R_{ps}$  which is defined as the ratio of the maximum principal stress to the critical failure stress  $\sigma_{cr}$  for an undamaged particle, and as the ratio of the current overall strain to the strain at



(a)



(b)

Fig. 7. Marked correlation function for (a) ratio of maximum principal stress to critical failure stress ( $\sigma_{cr}$ ), (b) average effective plastic strain in each Voronoi cells, for computer simulated microstructure.

which the particle had cracked, for a cracked particle ( $\frac{\sigma_c}{\sigma_{cr}} = 1$ ).  $R_{ps}$  signifies the propensity to advance the damage state in the microstructure; and (b) the average effective plastic strain  $\bar{\epsilon}^p$  in each Voronoi cell, which characterizes evolving matrix failure due to presence of damaged particles.

The marked correlation function  $M(r)$ , for which a mathematical formula is presented in [30], establishes the effect of microstructural morphology on the mark.  $M(r)$  for the two patterns and for a uniform microstructure ( $M(r) = 1$ ) are compared in Fig. 7. For the hard core pattern the functions rapidly decay to unity, but for the clustered patterns the decay is considerably slower. Higher  $M(r)$  values for clustered patterns at short range sampling distances  $r$  represent larger influence of the damage marks. The high value of  $M(r)$  for  $\bar{\epsilon}^p$  at short sampling distances indicates severe matrix straining near damaged particles. The slower attenuation of  $M(r)$  for  $R_{ps}$  at short to medium range indicates that particle cracking is a major mode of damage evolution. This function is effective in understanding the sensitivity of damage variables to local perturbations in the morphology, and can provide a criterion for determining the optimal RME size.

#### 4.2. Particle splitting simulation with actual micrographs

In this example, VCFEM analysis is conducted with micrographs obtained from serial sectioning of reinforced Al-Si-Mg alloys containing  $\approx 10$  or 20% by volume of Si particulates (see [29]). The material is developed at ALCOA Technical Center by rapid solidification of fine powders using a gas atomization process [22], to achieve equiaxed Si particles. The powder is consolidated by cold isostatic compaction, canned and degassed at 454°C, and finally consolidated to full density by hot isostatic pressing. Two types of microstructure are considered, viz. (a) a naturally aged 20% volume fraction composite with mean Si particle size of 4.4  $\mu\text{m}$ , and (b) a naturally aged 10% volume fraction composite with mean Si particle size of 3.9  $\mu\text{m}$ . Serial-sectioning of the specimens yield a series of 2-D sections as discussed in [29], which are then digitized.

**4.2.1. Characterization.** Equivalent microstructures that closely approximate the actual 2D morphology of micrographs and yet are computationally less intensive are generated. In this process each particle of arbitrary shape is replaced by an equivalent ellipse, constructed by equating the 0th, 1st and 2nd moments of the actual particles with those of the equivalent ellipses. The moments of actual particle are computed as the sum of moments of each pixel contained within the particle, while the moments of the ellipse are represented in terms of standard geometrical parameters. The procedure yields (i) the centroid ( $x_c$ ,  $y_c$ ), (ii) lengths ( $a$ ,  $b$ ) of the major and minor axes, and (iii) angular

orientation  $\theta$  of the major axis of the equivalent ellipse, details of which are discussed in Ref. [21]. An optical micrograph of a section, overlapped simulated and exact microstructures, and the Voronoi cell mesh obtained by surface to surface tessellation, are presented in Fig. 8(a), (b), and (c), respectively. Two sections of each volume fraction 10 and 20% are analyzed. The  $V_f = 10\%$  sections have 77 and 89 Si particles, while the  $V_f = 20\%$  sections contain 97 and 106 Si particles. A majority of computer results are explained with respect to sections of the 20%  $V_f$ , for which the microstructural element has dimensions of 205  $\mu \times 180 \mu$ , and the two-dimensional area fractions for the sections are calculated to be  $\approx A_f = 18.6\%$  and  $A_f = 18.9\%$ , respectively (note that the 3D  $V_f \sim 20\%$ ). Particle size distribution histograms (not shown) show considerable scatter within each section and also between sections. Cumulative ( $F$ ) and probability density distribution ( $f$ ) functions of the local area fraction ( $A$ ) and near-neighbor distance ( $d$ ) are plotted in Fig. 4(a), (b), (c) and (d). A comparison of the distribution functions in Fig. 4 reveals that the particle distribution is more in line with the hard-core pattern. Similar observations are also made in the plots of the second order intensity function  $K(r)$  and the pair distribution function in Fig. 4, where the absence of local peaks in  $g(r)$  signals negligible clustering. This observation is consistent with the material fabrication process in which the Si particulates are randomly precipitated from the mixture.

**4.2.2. Damage simulation.** Material properties of the constituents are: For the AL-Si-Mg matrix: Young's modulus  $E = 69$  GPa, Poisson's ratio  $\nu = 0.33$ , and the post yield elastic-plastic behavior (non-linear isotropic hardening) is obtained from data on T4-matrix presented in Fig. 8 of Kiser *et al.* [24]. For the Si inclusions: Young's modulus  $E = 161$  GPa, Poisson's ratio  $\nu = 0.2$  and mode I critical stress intensity factor for pure Si is found to be  $K_{IC} = 0.6$  MPa $\sqrt{\text{m}}$ . In the fracture mechanics approach for determining the size dependent critical fracture stress  $\sigma_{cr}$  in equation (9), the initial flaw size  $c$  is assumed to be proportional to the average equivalent particle diameter of  $D_{avg}$ . The proportionality constant  $e$  is calibrated by analyses of auxiliary RMEs created from micrographs of other sections of the specimen. A comparison is made between the computer simulations and experimental observations with micrographs for (a) the number of cracked particles and (b) overall stress-strain behavior. The estimate is obtained to be  $e = \frac{c}{D} = 0.125$  or 12.5%, and therefore the critical stress to fracture is taken to be

$$\sigma_{cr} = \sigma_{cr} = \frac{K_{IC}}{\sqrt{.125D\pi}}$$

For the approach with Weibull distribution, the two micrographs of 10%  $V_f$  are used for calculating

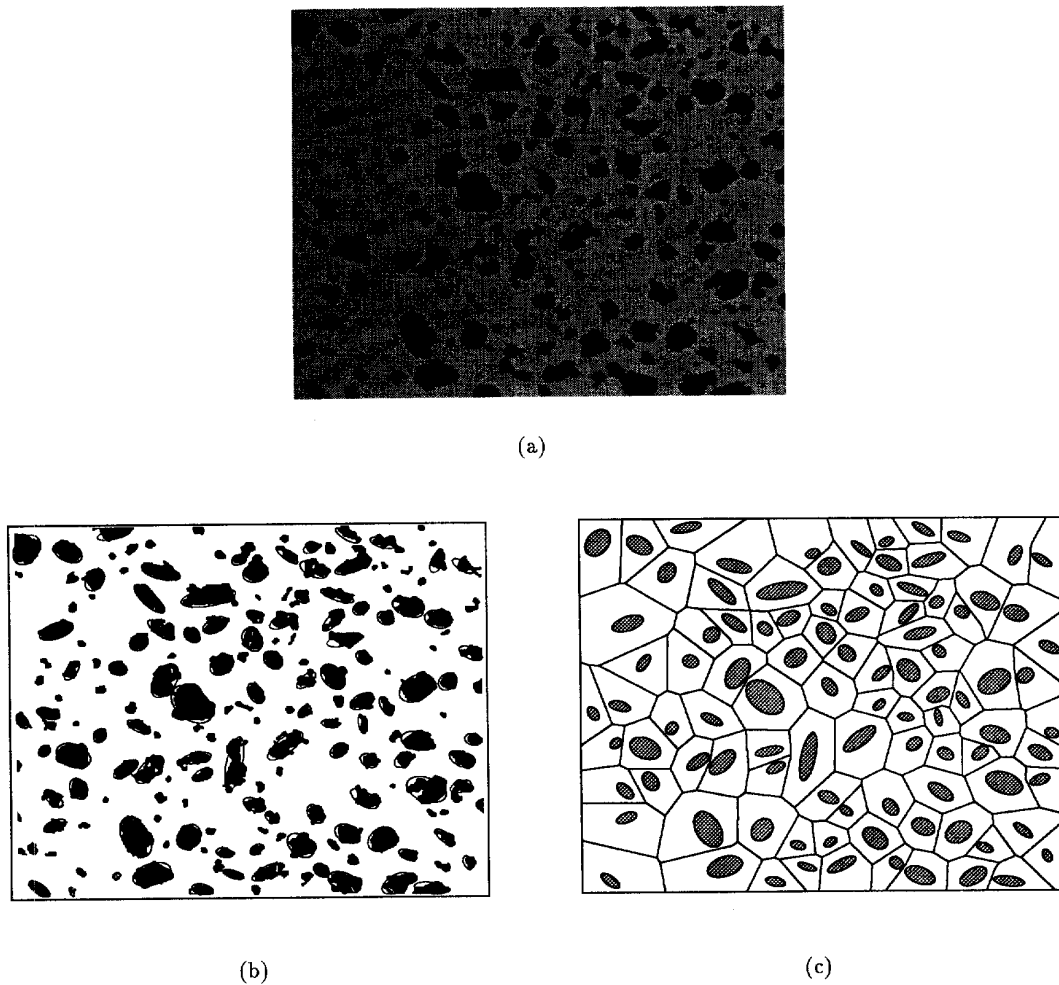


Fig. 8. (a) Optical micrograph of a section of Al-Mg-Si composite ( $\text{Si } V_f = 20\%$ ), (b) simulated microstructure superimposed on the micrograph and (c) Voronoi cell mesh resulting from tessellation.

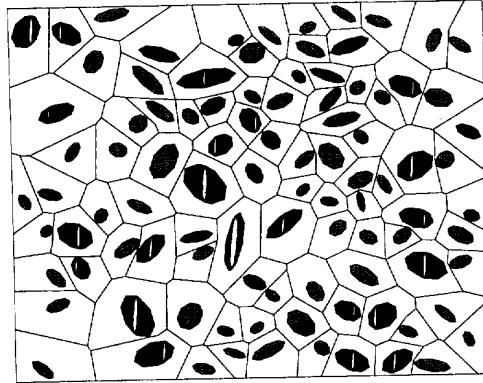
parameters  $\sigma_{cr}$  and  $m$ , since they exhibit the onset of particle cracking at  $\bar{\epsilon}_{xx} = 3\%$ . The cross-sectional area  $A$  of each individual particle is calculated from the data on ellipses in Fig. 8(d). The maximum principal stress  $\sigma_I$  at  $\bar{\epsilon}_{xx} = 3\%$  is obtained from VCFE analysis without any particle damage. The probability of failure  $P_f(A, \sigma)$  in equation (10) is assumed to be  $\geq 0.95$ . The Weibull parameters are evaluated to be  $m = 2.37$  and  $\sigma_{cr} = 2.12$  GPa, by comparison with the micrograph observations and by fitting the data in a least-square sense. The probability function  $P_f$  of individual particles indicates that both particle size and stress levels contribute independently towards cracking. A qualitative comparison between the two approaches for evaluating critical stress, is made by VCFEM analysis with the  $20\% V_f$  section of 97 particles strained to  $\bar{\epsilon}_{xx} = 6\%$ . Progression of damage in the microstructure with increasing strain is shown in Fig. 9(a), (b) and (c). Particles colored black are cracked while the grey particles are uncracked. A comparison of the frac-

tion of different sized particles that are cracked by each approach, is made with actual micrographic observation [Fig. 8(a)] in histograms [Fig. 9(d) and (e)]. The fractions for the actual micrograph are shown in grey with dashed outline. The histograms indicate that while both criteria are good for large particles, the Weibull distribution based approach provides a better agreement with the micrographs at the smaller size range. Hence, it is used in all subsequent simulations.

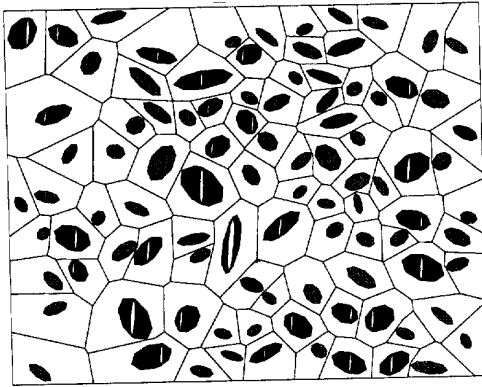
A damage parameter is defined as

$$\rho = \frac{\text{Area of Cracked Particles}}{\text{Total Area of All Particles}},$$

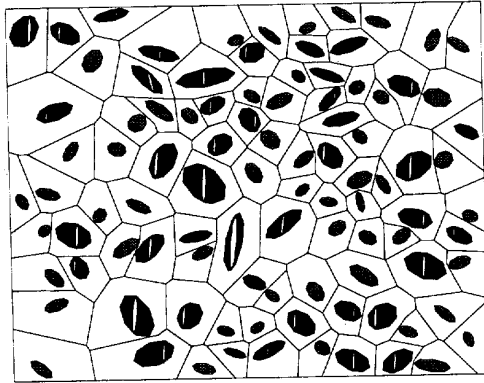
which accounts for size, is plotted in Fig. 10(a) for each of the two sections of the  $V_f = 10$  and  $20\%$  composites as a function of increasing strain. Experimental values of the corresponding damage parameter are given in Hunt [22], where the areas are calculated by sectioning after straining to a certain level. Consequently a single data point is



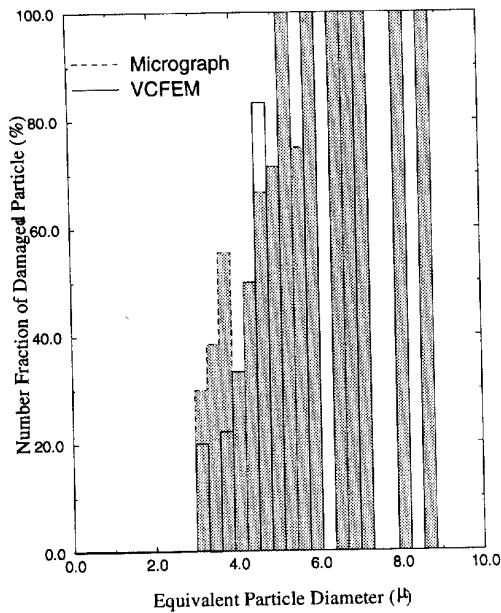
(a)



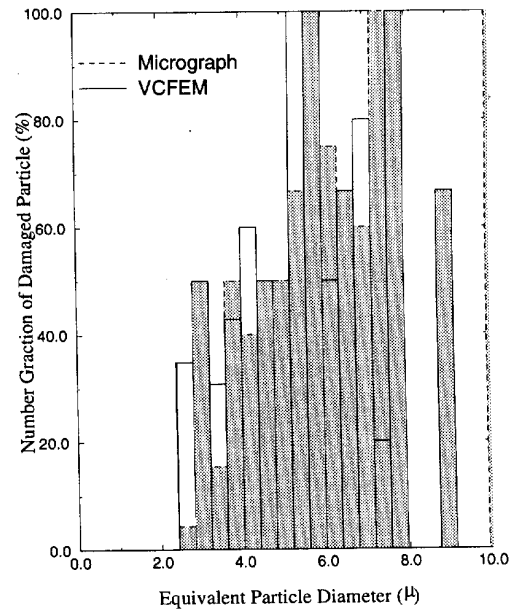
(b)



(c)



(d)



(e)

Fig. 9. Simulated configurations of evolving damage at (a)  $\bar{\epsilon}_{xx} = 3.0\%$ , (b)  $\bar{\epsilon}_{xx} = 4.2\%$  and (c)  $\bar{\epsilon}_{xx} = 6.0\%$  with a Weibull distribution based damage criterion; (d, e) histograms of number of damaged particles at  $\bar{\epsilon}_{yy} = 6\%$ , by Weibull distribution and fracture mechanics based damage criteria, respectively.

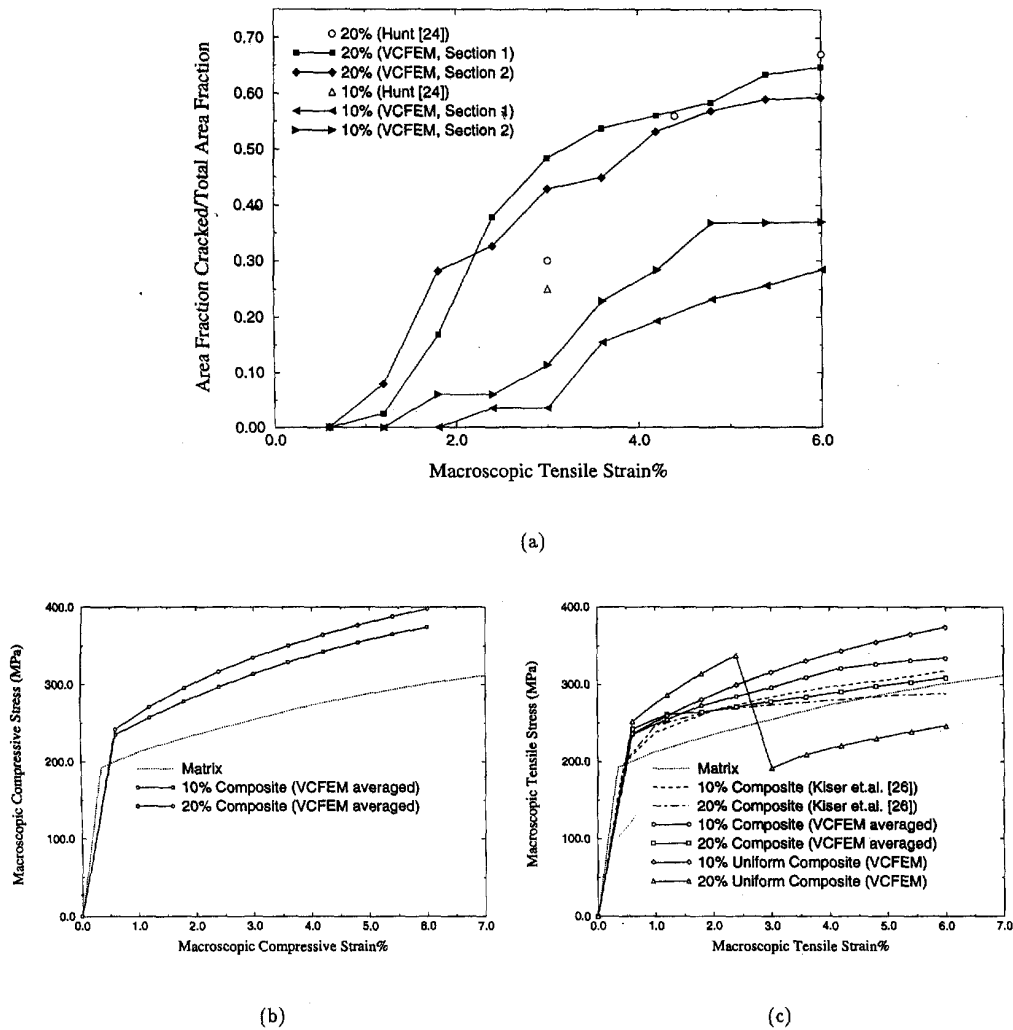


Fig. 10. (a) Area fraction of cracked particles as a function of the macroscopic strain. Macroscopic stress-strain response for the Al-Si-Mg composite microstructures at two volume fractions, (b) compressive response and (c) tensile response.

obtained from each specimen. Three experimental data points are plotted for the  $V_f=20\%$  composite, while the  $V_f=10\%$  has a single data point. Generally a good agreement is noted between simulated results and experimental data for the  $V_f=20\%$  composite. Stress-strain response of nearly undamaged microstructures are shown in Fig. 10(b) by loading RMEs in compression to an average strain of  $\bar{\epsilon}_{xx}=6\%$ . While the elastic response is not very different, the 20%  $V_f$  composite has higher yield stress and higher flow stress than the 10%  $V_f$  composite. The tensile response with particles cracking according to the Weibull criterion is shown in Fig. 10(c). Results of VCFEM analyses for each volume fraction are averaged over the two sections and are compared with experimental results of Kiser and Zok [24]. While VCFEM analysis is in 2D and the experimental results are for 3D, the

comparisons have a good qualitative agreement. The cross-over point at which the 20%  $V_f$  composite becomes less stronger than the 10%  $V_f$  composite, is approximately at  $\bar{\epsilon}_{xx}\approx 1.2-1.8\%$ , and compares well with the experimental value of  $\bar{\epsilon}_{xx}\approx 1.8\%$ . The stress capacity is in general higher for VCFEM predictions, which may be attributed to the constrained plastic flow arising from plane strain constraints. Additionally, the present simulation does not allow matrix softening which can also lower the load capacity. The stress-strain behavior of a uniform (square edge) microstructure with a single circular inclusion of volume fractions 10 and 20% is also plotted. The 10% uniform composite does not crack for the range of strains considered and predicts a stiff response. Failure of the single particle in the 20%  $V_f$  composite results in an abrupt drop

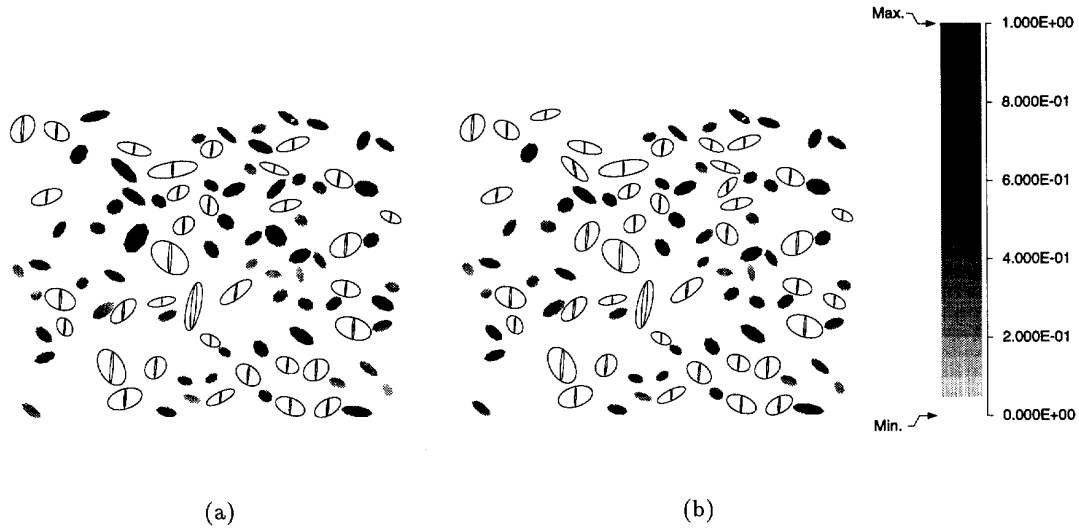


Fig. 11. Contour plots of particle fracture probability by the Weibull damage criterion immediately before: (a)  $\bar{\epsilon}_{xx}=4.2\%$  and (b)  $\bar{\epsilon}_{xx}=6.0\%$  for the Al-Si-Mg composite microstructure ( $V_f=20\%$ ). (Damaged particles are in white with cracks.)

in load capacity and yields unreasonable predictions.

Contour plots of particle failure probability and effective plastic strains for the 20%  $V_f$  composite are illustrated in Figs 11 and 12, respectively. Damaged particles are in white with cracks in Fig. 11, and the contour plots are for undamaged particles indicating the likelihood of damage. An interesting observation made from these plots is that some large particles which exhibit a higher tendency to crack at early stages of loading, may remain intact throughout due to failure of neighboring particles and load redistribution. This phenomenon, also noticed with particle clusters in the previous

example, illustrates the influence of evolving microstructural morphology on the propagation of damage. A particle crack induces large plastic flow in the neighboring matrix which causes the stress to rise in particles in this region and eventually initiate a crack. The plastic strain distribution in Fig. 12(a) shows localized bands of severe deformations emanating from crack tips and propagating to neighboring particles with cracks. The remainder of the matrix undergoes relatively smaller deformations. Marked correlation functions  $M(r)$  are plotted in Fig. 13 as functions of distance and particle shapes, for the two sections of 20%  $V_f$  composite. Two marks viz. (a) particle fracture probability  $P_f$  and

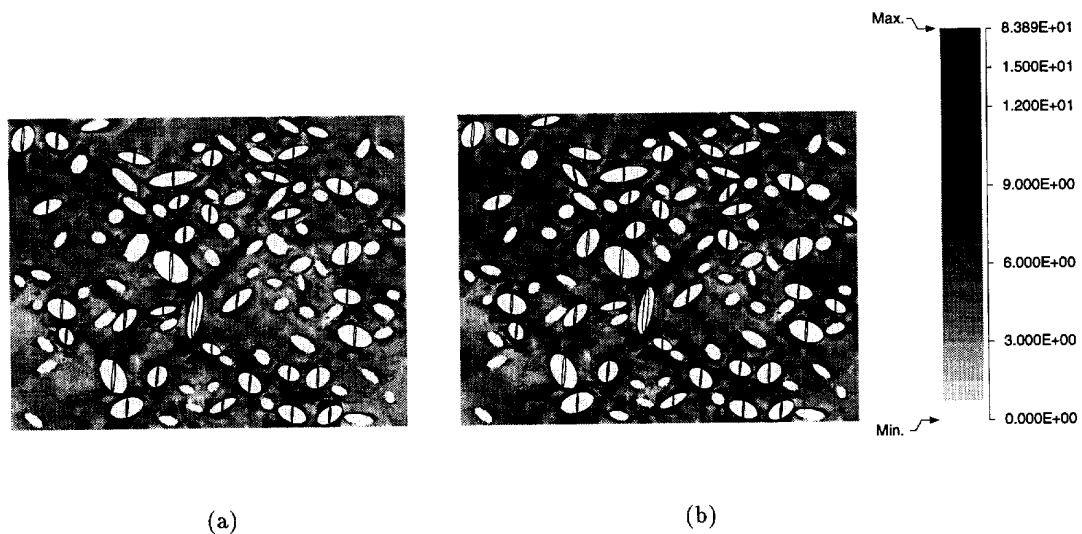


Fig. 12. Effective plastic strain (%) contours at (a)  $\bar{\epsilon}_{xx}=4.2\%$  and (b)  $\bar{\epsilon}_{xx}=6.0\%$  for the Al-Si-Mg composite microstructure ( $V_f=20\%$ ).

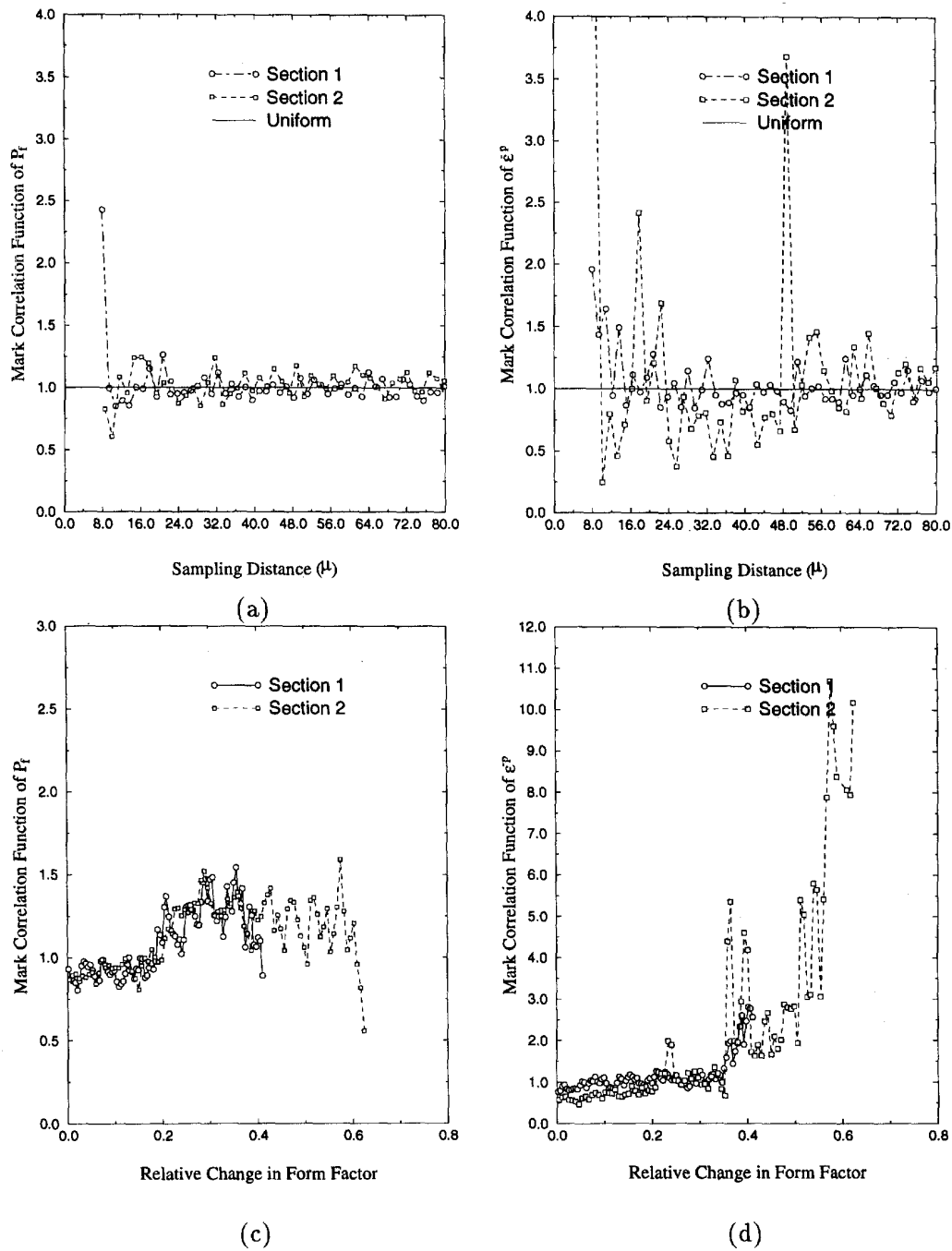


Fig. 13. Marked correlation functions of (a) failure probability and (b) average effective plastic strain in each Voronoi cell as a function of radial distance, and marked correlation functions of (c) failure probability and (d) average effective plastic strain in each Voronoi cell as a function of form factor; for the Al-Si-Mg composite microstructure ( $V_f=20\%$ ).

(b) effective plastic strain  $\bar{\epsilon}^p$  are selected as qualitative indicators of microstructural damage. Uniform  $M(r)$  plots of unit value occur for regular patterns and correspond to identical marks. Figure 13(a) and (b) of  $M(r)$  with respect to the sampling distance  $r$  shows that the functions for  $P_f$  quickly

stabilize near the unit value, while the decay is slower for  $\bar{\epsilon}^p$  with a few abrupt peaks. The lack of strong clustering in these patterns leads to smaller influence regions for these microstructures. Marked correlation functions with respect to the relative difference in form factors  $F_f$  are plotted in Fig. 13(c)



and (d). The form factor is an indicator of the deviation in shape from a perfect circle ( $F_f = 1$ ), and for an elliptical shape, may be expressed as (see [28]):

$$F_f = \frac{4\pi R^2}{\text{perimeter}^2}; R = \sqrt{ab};$$

$$\text{perimeter} \approx \pi \left[ 1.5(a + b) - \sqrt{ab} \right] \quad (11)$$

where  $a$  and  $b$  are the major and minor axes. The maximum observed form factor  $F_f$  is computed to be 0.97 while the minimum is 0.48. Figures 13(c) and (d) depict increasing correlation functions especially for  $\bar{\epsilon}^p$ . This infers that shape has a significant influence on the damage in these microstructures.

### 5. CONCLUSIONS

This paper is devoted to stress analysis of non-uniform, ductile matrix composite microstructures with particle cracking, by the Voronoi cell finite element method (VCFEM). The computational model assumes complete cracking at the onset of damage, and differentiates between the behavior of fully cracked particles and split particles. The uniqueness of this model lies in its ability to model continuously changing element topology due to progressive material failure, with no user interference. Validation of the computation model for damage is done through various studies, including comparison with other numerical studies in the literature that use conventional finite element codes. These studies have predominantly analyzed simple uniform distributions with pre-existing cracks. Good agreement is obtained in these comparison studies, both from a macroscopic and microscopic point of view.

A major advantage of VCFEM is that it can be used for analyzing damage in non-uniform real micrographs without making major morphological simplifications. A set of computer generated hard-core and clustered microstructures are simulated to understand the effect of spatial distribution on damage evolution. Damage initiates within each cluster, propagates within the cluster and finally links up with the damage in the neighboring clusters. Regions of severe plastic flow exist in the matrix ahead of split particles, indicating possible sites of matrix failure. Particle splitting is found to yield much softer overall response than particle cracking. In a concluding example, the VCFEM model is directly constructed from a digitized optical micrograph of an Al-Si-Mg composite system. VCFEM results are compared with results of experiments with this material for two volume fractions. Good concurrence is obtained in the overall stress-strain behavior, as well as in the number of damaged particles in the microstructure. Larger particles tend to fail at lower loads and therefore serve as sites of damage initiation. Nevertheless,

smaller particles may also damage with loading, due to stereological factors like proximity with other particles and relative shape. It is noted that damage evolution in real microstructures is a gradual process, and takes place by progressive particle failure. Material behavior is therefore misrepresented with the single cell models where particle cracking results in abrupt changes in response. Statistical descriptors are used as indicators of morphological influence on the damage state. The efficiency of the VCFEM codes is noteworthy. A comparison with conventional FEM packages for undamaged-non-uniform and damaged-uniform materials shows a ~30–50 times reduction in computing time. Currently, matrix cracking phenomenon is being incorporated in VCFEM and this will be reported in future.

*Acknowledgements*—The authors would like to thank O. Richmond, H. Weiland, and T. R. Rouns of ALCOA Technical Center for their help on the experimental portion of this work. This work has been sponsored by the Mechanics and Materials program (Program Director S. Saigal) of National Science Foundation through a NSF Young Investigator grant (Grant No. CMS-9457603), and by the United States Army Research Office through Grant No. DAAH04-95-1-0176 (Program Director: K. R. Iyer). Computer support was provided by the Ohio Supercomputer Center through grant #PAS813-2.

### REFERENCES

1. Brechet, Y., Embury, J. D., Tao, L. and Luo, L., *Acta metall. mater.*, 1991, **39**, 1781.
2. Christman, T., Needleman, A. and Suresh, S., *Acta metall. mater.*, 1989, **37**, 3029.
3. Hashin, Z., *J. Mech. Phys. Solids*, 1988, **36**, 719.
4. Chen, Y.-Z., *Eng. Fract. Mech.*, 1984, **38**, 379.
5. Lacy, T. E., McDowell, D. L. and Willice, P. A., *ASTM*. Submitted for publication.
6. Shih, C. F. and Asaro, R. J., *J. Appl. Mech.*, 1989, **56**, 763.
7. Evans, A. G., Dagleish, B. J., He, M. Y. and Hutchinson, J. W., *Acta metall. mater.*, 1989, **37**, 3249.
8. Needleman, A., *J. Appl. Mech.*, 1987, **54**, 525.
9. Needleman, A., *J. Mech. Phys. Solids*, 1990, **38**, 289.
10. Tvergaard, V., *J. Mech. Phys. Solids*, 1991, **41**, 1309.
11. Bao, G., *Acta Metall. Mater.*, 1992, **40**, 2547.
12. Hom, C. L., Mataga, P. A. and McMeeking, R. M., *Int. J. Numer. Meth. Engng.*, 1989, **27**, 233.
13. Sugimura, Y., Lim, P. G., Shih, C. F. and Suresh, S., *Acta metall. mater.*, 1995, **43**, 1157.
14. Finot, M., Shen, Y.-L., Needleman, A. and Suresh, S., *Metall. Mat. Trans. A*, 1994, **25A**, 2403.
15. Brockenbrough JR, Suresh, S. and Weinecke, W. A., *Acta metall. mater.*, 1991, **39**, 735.
16. McHugh, P. E., Asaro, R. J. and Shih, C. F., *Acta metall. mater.*, 1993, **41**, 1461.
17. Moorthy, S. and Ghosh, S., *Int. J. Numer. Meth. Engng.*, 1996, **39**, 2363.
18. Ghosh, S. and Moorthy, S., *Comp. Meth. Appl. Mech. Engng.*, 1995, **121**, 373.
19. Moorthy, S. and Ghosh, S., *Comp. Meth. Appl. Mech. Engng.*, in press.
20. Muskhelishvili, N. I., *Some Basic Problems in the Mathematical Theory of Elasticity*, P. Nordhoff, 1965.

21. Moorthy, S., Ph.D. thesis, Ohio State University, 1997.
22. Hunt, W. H.. Thesis, Carnegie Mellon University, 1992.
23. Hunt, W. H., Brockenbrough JR and Magnusen, P. E., *Scripta metall. mater.*, 1991, **25**, 15.
24. Kiser, M. T., Zok, F. W. and Wilkinson, D. S., *Acta metall. mater.*, 1996, **9**, 3465.
25. Curtin, W. A., *J. Amer. Cer. Soc.*, 1994, **77**, 1075.
26. Brockenbrough JR and Zok, F. W., *Acta metall. mater.*, 1993, **40**, 2547.
27. Ghosh, S., Nowak, Z. and Lee, K., *Acta metall. mater.*, 1997, **45**, 2215.
28. Ghosh, S., Nowak, Z. and Lee, K., *Comp. Sci. Tech.*, in press.
29. Li, M., Ghosh, S., Rouns, T. N., Weiland, H. and Richmond, O. submitted for publication.
30. Pyrz, R., *Comp. Sci. Tech.*, 1994, **50**, 197.